Dipolarization Events With Inductive, Radial Electric Fields Observed by Van Allen Probes

H. Matsui[1], R. B. Torbert[1], H. E. Spence[1], M. B. Cooper[2], C. J. Farrugia[1], M. Gkioulidou[3], T. J. Metivier[1], and J. R. Wygant[4]

[1]Space Science Center, University of New Hampshire, Durham, NH, USA
[2]Center for Solar-Terrestrial Research, New Jersey Institute of Technology, Newark, NJ, USA
[3]The Johns Hopkins University Applied Physics Laboratory, Laurel, MD, USA
[4]School of Physics and Astronomy, University of Minnesota, Minneapolis, MN, USA

Key Points:

- Dipolarization events with inductive, radial electric fields were observed in the dusk-side with energetic proton increases.
- Magnetic field lines were often stretched with their motion similar to the gradient B/curvature drift velocities of energetic protons.
- These events could be due to drifting, energetic proton structures and accompany standing wave signatures.

Corresponding author: H. Matsui, `hiroshi.matsui@unh.edu`

Abstract

Dipolarization events with inductive, radial electric fields are examined, using Van Allen Probes data between 2013 and 2018. Two cases are studied, followed by statistical analyses. These events were observed between evening and premidnight magnetic local times (MLTs) under moderate geomagnetic activities. Radial electric field variations, azimuthal magnetic field variations, and energetic protons were often observed when horizontal magnetic fields started to decrease in the dip region. Magnetic field lines were stretched with their motion similar to the gradient B/curvature drift velocities of energetic protons. Signs of electric fields changed when horizontal magnetic fields started to increase in the dipolarization front (DF). Electric field variations were correlated with magnetic field ones with ~ 90 deg. phase shift. These observations are mainly interpreted in terms of energetic proton structures drifting toward the probe locations, while being accompanied by standing waves.

1 Introduction

Dipolarization events of geomagnetic fields have often been reported in the nightside magnetosphere since the 1960's (Cummings et al., 1968; McPherron et al., 1973). Geomagnetic fields typically stretched tailward return to the original dipolar shape during these events. They have often been observed during geomagnetically active periods such as substorms. These events have not only been observed around geosynchronous orbit (e.g., Nagai, 1982), but also in the magnetotail (e.g., Nakamura et al., 2002). These events have been thought to originate from magnetotail reconnection and subsequently propagate earthward. Hall electric fields are formed due to different gyroradii between ions and electrons around the dipolarization front (DF) (Runov et al., 2011). There are reviews on this topic (Sergeev et al., 2012; Kepko et al., 2015). These events have also been observed inside geosynchronous orbit, e.g., by Van Allen Probes (Gkioulidou et al., 2015; Liu et al., 2016). Since background geomagnetic parameters are different from those of the magnetotail, characteristics of the dipolarization events in the inner magnetosphere could also be different.

Dipolarization events are often associated with particle injections. A relation to energetic protons was examined by Baker et al. (1979). Birn et al. (1997) showed that ion injections were shifted duskward, while electron injections were shifted dawnward. Gkioulidou et al. (2015) presented a detailed analysis of multiple dipolarization events

on a Van Allen Probe B's orbit. There were various spatial scales $\sim 2-5$ h in magnetic local time (MLT). Energetic proton fluxes behaved differently depending on energy during dipolarizations. Liu et al. (2016) demonstrated that half of dipolarization events inside geosynchronous orbit were observed with energetic particle injections. In these events, the observed electric fields were larger. Motoba et al. (2021) showed a superposed epoch analysis of energetic particle injections and dipolarizations. When the energetic proton fluxes started to increase, the horizontal magnetic field decreased in some cases, which could be due to a diamagnetic effect. That proton increase was possibly due to reflected populations at the DF, observed and modeled in the magnetotail (Zhou et al., 2014).

There have been reports that ultra low frequency (ULF) waves were observed during dipolarization events. These waves could have standing wave signatures (Takahashi et al., 1988). Kinetic scales could be involved (Chaston et al., 2014). The Poynting flux may provide energy source for aurora (Ergun et al., 2015). Nightside ground observations of field line resonances were examined during substorm intensifications (Samson et al., 1992). These waves were inferred to be kinetic and occur in the dipolelike region of the magnetosphere, outside the plasmapause. In addition, ULF waves were observed in the plasmasheet boundary layer during a dipolarization event (Tian et al., 2021).

We have previously reported a dipolarization event observed by Magnetospheric Multiscale (MMS) in the inner magnetosphere (Matsui et al., 2016). Energetic ions were enhanced in the dip region before the start of the dipolarization, which could cause inductive, radial electric fields or standing waves. A limitation of that study was that the particle measurement was only performed in a high energy range above tens of keV because low energy particle instruments were not operational. Here we analyze dipolarization events observed by Van Allen Probes, by which particle measurements were performed in a wide energy range in the inner magnetosphere (Mauk et al., 2013). We may examine the relationship between particles and fields in more detail. In addition, plenty of data are available after the completion of the mission so that a statistical analysis may be made. The objective of this study is to investigate dipolarization events with inductive, radial electric fields in terms of their physical properties. Here we show an analysis for two events and statistical results.

This paper is organized as follows. In Section 2, we describe data to be analyzed. In Section 3, two case studies are presented. Statistical analyses follow in Section 4. Summary and conclusions are discussed in Section 5.

2 Data

We analyze field and particle data measured by Van Allen Probes (Mauk et al., 2013) between 2013 and 2018. Van Allen Probes had equatorial orbits with magnetic latitudes (MLATs) within 20 deg. from the magnetic equator. The perigee was 1.1 R_E of the geocentric distance, while the apogee was 5.8 R_E so that observations were performed in the inner magnetosphere. There were two probes A and B with slightly different orbits and therefore the interprobe separation was variable. Orbital periods were $\sim$ 9 h.

Magnetic fields were measured by Electric and Magnetic Field Instrument Suite and Integrated Science (EMFISIS) (Kletzing et al., 2013). We use 1-s data. Electric fields were measured by Electric Field and Waves (EFW) Instruments (Wygant et al., 2013). 32-Hz data are averaged to 1-s resolution for the analysis. We examine high-energy proton data with energies between 40 and 600 keV, measured by Radiation Belt Storm Probes Ion Composition Experiment (RBSPICE) (Mitchell et al., 2013). Spin-averaged, 11-s flux and moment data (Pitch Angle and Pressure TOF x Energy Proton Rates, PAP_TOFXEH) are analyzed. High-energy electron fluxes with energies between 30 keV and 4 MeV were measured by Magnetic Electron Ion Spectrometer (MagEIS) (Blake et al., 2013) with 11-s resolution. This instrument also measured ions with energies between 60-160 keV and 1.3 MeV, complementing the RBSPICE measurements. Low-energy proton and electron fluxes with energies between 1-15 eV and 50 keV were measured by Helium, Oxygen, Proton, and Electron (HOPE) Mass Spectrometer (Funsten et al., 2013) nominally with 22-s resolution. Proton moment data were calculated in the energy range above 30 eV.

Geomagnetic activities are monitored by auroral electrojet (AE), Kp (Matzka, Stolle, et al., 2021), and Dst indices, while interplanetary parameters are examined by OMNI data (King & Papitashvili, 2005).

3 Event Studies

In this section we show two dipolarization events. Although both events are common in that dipolarization is accompanied by electric field variations and energetic proton injections with similar timing, the details are not necessarily similar. Therefore, we will be able to illustrate these dipolarization events further by showing two events.

3.1 A Dipolarization Event on 19 July 2013

There was a dipolarization event starting at 18:03:58 UT on 19 July 2013, as observed by Van Allen Probe A. The probe was located at L=5.5, 19.4 MLT, and MLAT=9.5 deg. Note that an event is considered to start as the horizontal magnetic fields in VDH coordinates, subtracted by modeled magnetic fields B_{T89Q} by Tsyganenko (1989) during quiet periods (Kp=0), start to increase. Here, cylindrical, VDH coordinates are defined as follows: V in the outward direction, D in the eastward direction, and H in the northward direction along the dipole axis.

This event did not correspond to a geomagnetic storm ($Dst = -21$ nT). The geomagnetic activity monitored by the Kp index was moderate with 4^-. There was some auroral electrojet activity ($AU = 254$ nT and $AL = -284$ nT). This could be explained by the OMNI data in which the interplanetary magnetic field (IMF) was quite often southward for the preceding several hours or even longer.

Figure 1 shows an overview plot for magnetic fields and electric fields, followed by energetic proton fluxes and pressure measured by RBSPICE. Magnetic pressure is added in the bottom panel of plasma pressure. Quiet-time, modeled magnetic fields B_{T89Q} are plotted with measured ones in the top three panels and did not change much during the plotted interval of 10 min because Probe A was close to apogee.

The B_H component decreased between 18:02:32 and 18:03:58 UT, noted as the dip region, and increased between 18:03:58 and 18:07:40 UT, noted as the DF. The terms, dip and DF, have been used in other studies (e.g., Schmid et al., 2019). Each of the above times are indicated by vertical guidelines. After the dipolarization, the measured magnetic field was closer to the quiet-time, modeled magnetic field, i.e., dipolar configuration. The B_D component increased in the dip and then decreased in the DF. Since Probe A was located in the northern hemisphere, this variation corresponds to the magnetic

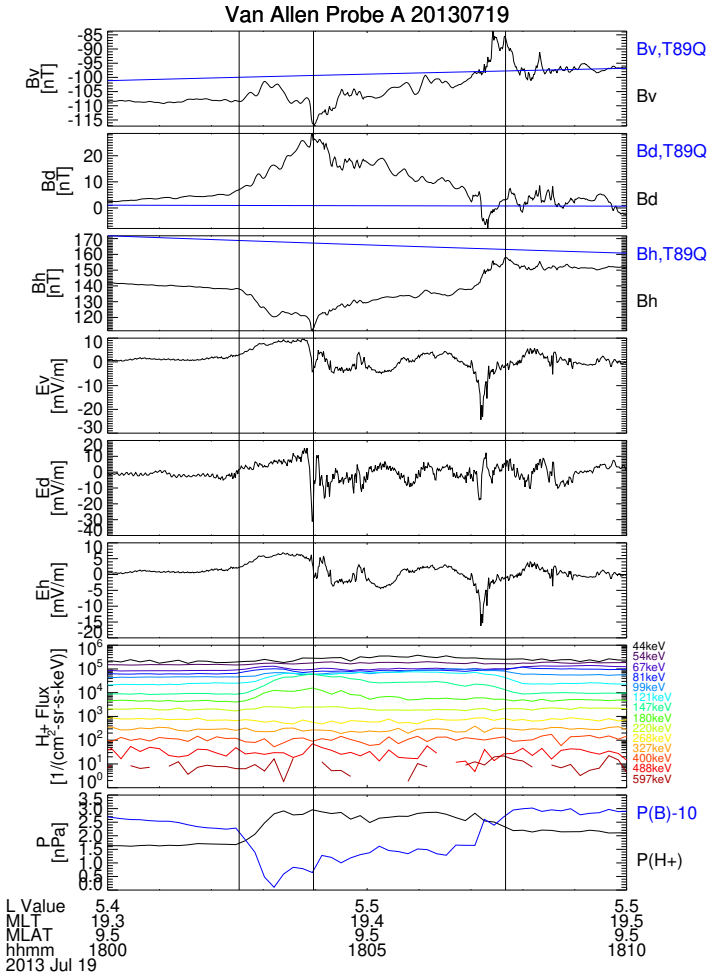

Figure 1. An overview plot for a dipolarization event starting at 18:03:58 UT on 19 July 2013, as observed by Van Allen Probe A. Three components of magnetic fields and electric fields in VDH coordinates and energetic proton fluxes and pressure measured by RBSPICE are plotted from top. Modeled magnetic fields B_{T89Q} are overlaid in the top three panels. Magnetic pressure is added in the bottom panel. Three vertical lines indicate beginning of the dip, ending of the dip or beginning of the DF, and ending of the DF.

field line displaced westward in both the dip and DF. This might imply inward current, although there is another term related to horizontal magnetic field variations in the azimuthal direction. If static, the inward current indicates westward pressure gradient and therefore the field-aligned current (FAC) toward the ionosphere, which could constitute Region 2 (R2) current in the evening sector. The B_V component overall decreased and increased in the dip and DF, respectively. Together with the behavior of the B_H com-

ponent, it is inferred that the magnetic field line was stretched outward and then compressed inward.

In the dip region, each electric field component became positive and then approached to $\sim$ 0 mV/m, while each magnetic field component increased or decreased to have a peak value near the end. We may consider that there was a phase shift $\sim$ 90 degrees between electric field and magnetic field variations, taking into account field variations afterwards as well. The correspondence between electric and magnetic field variations implies electric fields were inductive. Vertical and horizontal electric fields increased by $\sim$ 10 and $\sim$ 5 mV/m, respectively. Magnetic field lines were stretched westward, consistent with the B_D variation mentioned above. Electric field variations were larger than typical background convection electric fields of $<\sim$ 1 mV/m. There was also an eastward electric field increase, indicating field lines were moving outward. After that each component of electric fields changed its sign with lots of fluctuations in the DF. Magnetic field lines overall moved back eastward and inward.

Energetic proton fluxes also increased at $\sim 45-210$ keV in the dip region. Plasma pressure increased by 1.2 nPa, while magnetic pressure decreased by 1.5 nPa. Total pressure was approximately conserved. The equatorial gradient B drift speed of 75 keV protons under the dipole magnetic field at the L shell of Probe A, 5.4, is $\sim$ 30 km/s, which is similar to the measured, westward component of the $E \times B$ drift speed $\sim$ 50 km/s. Note that the curvature drift speed at the same energy is double of the gradient B drift speed with the same approximation. In the DF, plasma pressure decreased. At this time, magnetic pressure increase was larger than plasma pressure decrease.

Figure 2 is an overview plot for particle measurements during this dipolarization event, together with the B_H component for reference. When energetic proton fluxes $>\sim$ 50 keV increased, those $\sim 10-30$ keV decreased. Nonetheless, contribution to the pressure from the former component was larger (discussed later). Electron fluxes increased as the background magnetic field increased. There was no specific injection signature in the dip region, contrary to the ions.

3.2 A Dipolarization Event on 9 June 2015

Another dipolarization event started at 22:52:07 UT on 9 June 2015. Van Allen Probe A was located at $L = 6.0$, 19.3 MLT, and MLAT=11.1 deg. Some auroral electrojet

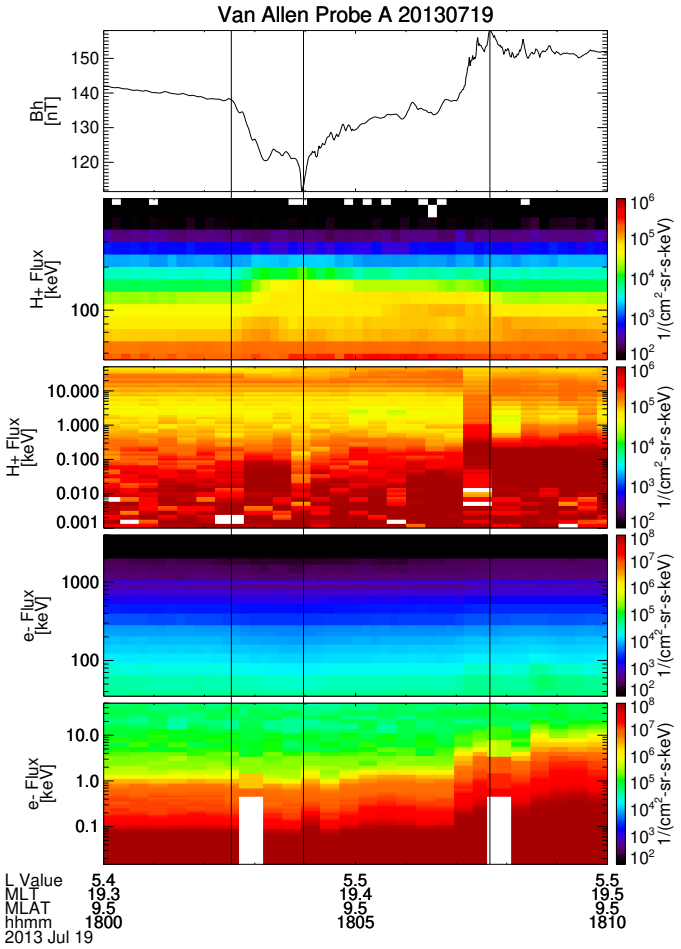

Figure 2. An overview plot for particle measurements during a dipolarization event starting at 18:03:58 UT on 19 July 2013. From top, the B_H component, high-energy proton fluxes from RBSPICE, low-energy proton fluxes from HOPE, high-energy electron fluxes from MagEIS, and low-energy electron fluxes from HOPE are plotted. Proton and electron fluxes from two instruments are plotted with a common color scale, respectively. Three vertical lines indicate the same times as in Figure 1.

activity started at 22:47 UT. AU and AL values reached 279 and -275 nT, respectively, at 22:52 UT. The Kp value was moderate with 2^+. This event corresponded to the recovery phase of a corotating interaction region (CIR)-driven geomagnetic storm. The minimum Dst value was -67 nT at 8 UT on the previous day. After that Dst values gradually recovered. At the time of the dipolarization, the value was -28 nT. The IMF was fluctuating due to the CIR encounter. The B_Z component was ~ -3 to 0 nT around the time of the event.

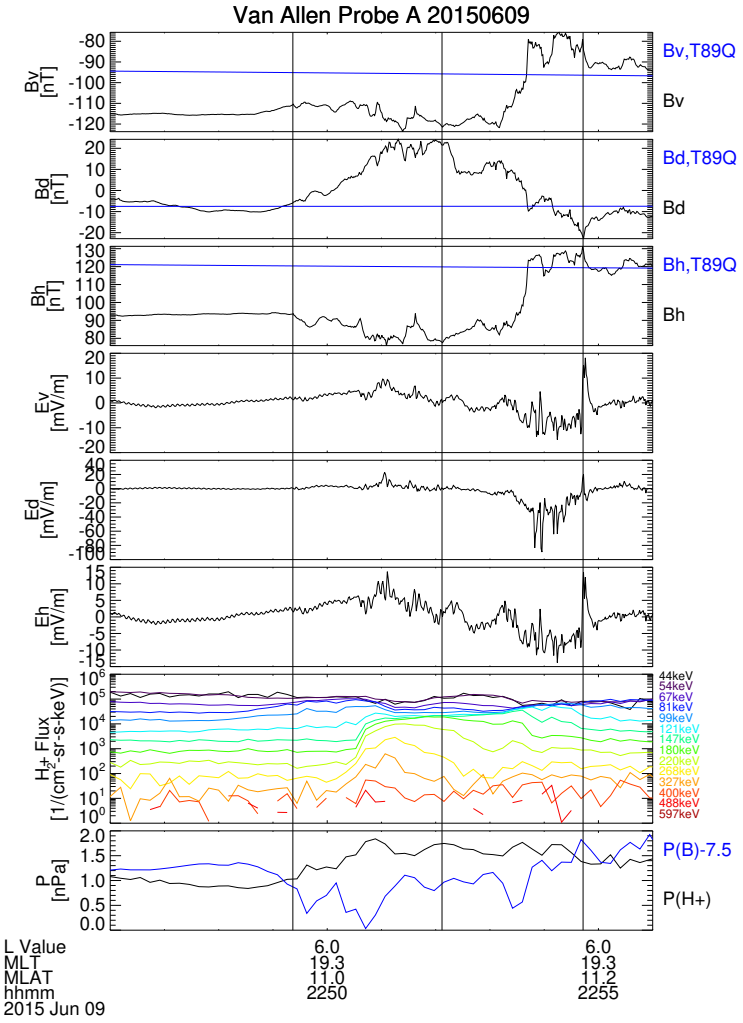

Figure 3. An overview plot for a dipolarization event starting at 22:52:07 UT on 9 June 2015, as observed by Van Allen Probe A. Magnetic fields, electric fields, and energetic protons are plotted in the same format as in Figure 1. Three vertical lines correspond to beginning of the dip, ending of the dip or beginning of the DF, and ending of the DF, respectively.

Figure 3 is an overview plot for magnetic and electric fields together with energetic protons for this event. The northward magnetic field B_H started to decrease at 22:49:22 UT and reached minimum $\sim$ 22:52:07 UT, including some fluctuations. This interval corresponds to the dip region. After that the B_H component increased to the maximum at 22:54:43 UT, corresponding to the DF. The azimuthal magnetic field B_D increased in the dip, while decreased in the DF. Since Probe A was located in the northern hemisphere, the field line was displaced westward.

There were, again, electric field variations concurrent with magnetic field variations. Outward and northward components were observed in the dip, while their signs were reversed in the DF. These correspond to westward and eastward motion of magnetic field lines in the dip and DF, respectively. Westward electric field or outward motion was observed in the dip, while larger, eastward electric field or inward motion was observed in the DF.

Energetic proton pressure increased in the dip, while magnetic pressure was smaller than neighboring values. In the DF, proton pressure decreased somewhat, while magnetic pressure increased more than that decrease.

It appears that the proton flux increased in two steps. The first increase started gradually at $\sim$ 22:48 UT in the middle energy range of $\sim 80 - 100$ keV. The second increase was sharper and started at $\sim$ 22:50 UT near the minimum B_H at the energy of $\sim 120{-}400$ keV. These were similar to the observations by Gkioulidou et al. (2015) and Motoba et al. (2021). Even though the second increase was sharp and at high energies, the pressure increase was larger at the first increase, due to the larger energy flux of the middle energy component.

One possible reason for the two-step increase is that the energetic population within a dipolarization structure consists of two parts. The one around the minimum B_H was possibly related to the local dipolarization process, while another with the middle-energy flux increase was due to the flux reflected at the DF (Zhou et al., 2011), as suggested by Motoba et al. (2021). Reflected flux may be observed of the order of the ion gyroradius from the DF where such reflection occurs. Here we estimate typical values of equatorial gyroradius and gradient B drift speed as 310 km and 49 km/s, respectively, at the L value of 6.0 where probe A was located, assuming particle energy of 90 keV and the dipole field. Probe A would traverse a structure with the gyroradius $\sim$ 6 s, which is much shorter than the duration of the dip of the order of minutes. Here we assume that motion of the structure is of the order of the gradient B drift speed. There was not a significant proton flux increase $>\sim$ 100 keV, at which the gyroradius is closer to the dip length so that it is hard to explain the duration of the dip by local reflection.

Enhanced ions at $\sim 80{-}100$ keV may not be locally reflected at the DF but propagate from the magnetotail, where these ions were perhaps reflected. In order to examine this possibility, we refer to the observation reported by Zhou et al. (2011). Particle

fluxes of several tens of keV were enhanced in the magnetotail. The duration of the dip could be explained by gyroradius of these ions divided by inward propagation velocity there. If the magnetic moment is conserved during the transport process from the magnetotail to the Probe A's orbit, the perpendicular energy would be at most several keV, while the parallel energy would be just below the original $\sim 80-100$ keV, which is not so realistic. Therefore, the pitch angle and possibly energy would change during the transport process. Nonetheless, the ion flux in the dip observed by Probe A could be generated by the reflection process in the magnetotail. The longer duration of the dip in the inner magnetosphere will be discussed again later.

The previous event on 19 July 2013 did not clearly show the two-step increase like this event. Nonetheless, the peaks of the middle energy and high energy fluxes were slightly offset in time. One possible reason for this is that the thickness of the dipolarization structure or its shape is different depending on the probe location relative to its center.

Figure 4 shows the particle measurements in detail. Particle signatures were overall similar to those on 19 July 2013. When energetic proton fluxes $>\sim 60$ keV increased, those around a few tens of keV decreased. Nonetheless, contribution to the pressure from the former component was larger. Electron fluxes increased as the background magnetic field increased.

For this event, Van Allen Probe B was located close to Probe A and observed the dipolarization as well (Figure 5). The probe location was $L = 5.9$, 19.6 MLT, and MLAT=10.8 deg. at 22:52:07 UT, when the dipolarization event started at Probe A. Probe B was located inward with $dL = -0.1$ and 0.3 h eastward in MLT. Although there were gaps in electric field data, variations in magnetic fields, electric fields, and energetic protons were similar to those observed by Probe A. Therefore, the spatial scale of the structure was at least the separation distance between these two probes. There was a tendency for Probe B to observe the dip and DF around several to several tens of s earlier than Probe A, which could be explained by a westward propagation of the event.

4 Statistical Studies

In this section, we statistically analyze various properties of dipolarization events with inductive, radial electric fields. Properties discussed include spatial occurrence, field variations, pressure variations, and durations. We have collected a total of 22 events with

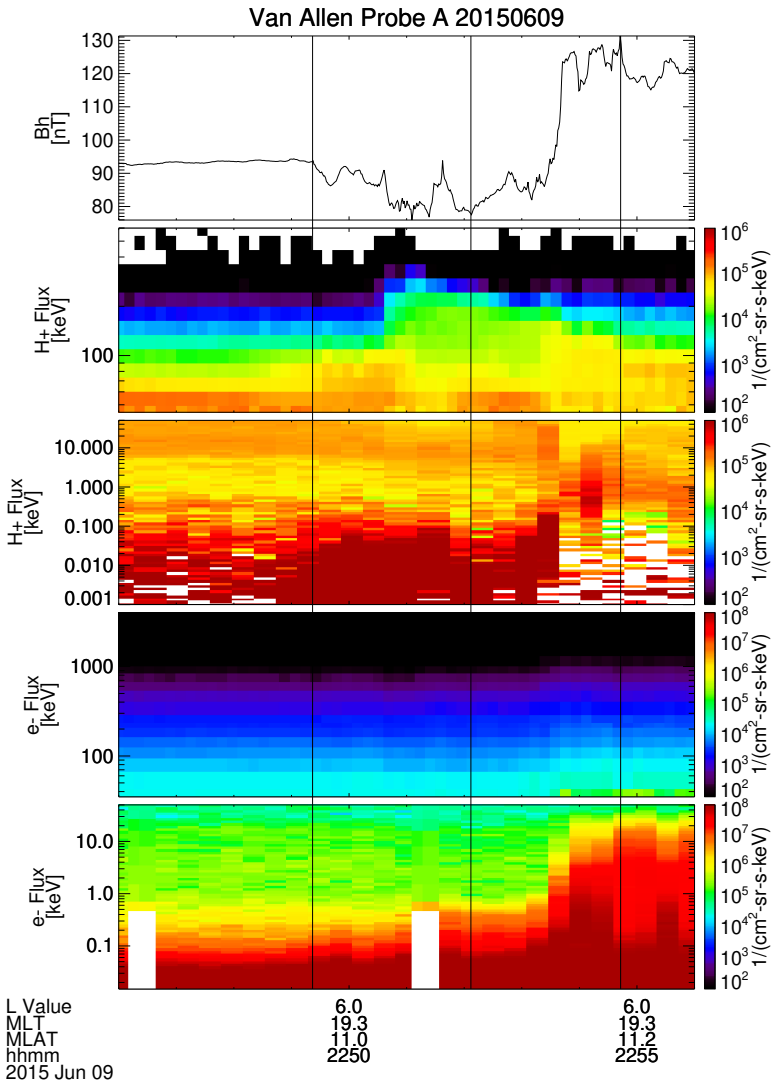

Figure 4. An overview plot for particle measurements for a dipolarization event starting at 22:52:07 UT on 9 June 2015. Horizontal magnetic fields B_H and proton and electron fluxes are plotted in the same format as in Figure 2. Three vertical lines indicate the same times as in Figure 3.

horizontal and vertical electric fields correlated with azimuthal magnetic fields with ∼ 90 deg. phase shift around the dipolarizations. These events are listed in the supporting information.

First, the spatial occurrence of these events are examined (left three panels of Figure 6). All events were observed between evening and premidnight MLTs. If energetic protons are related to this type of dipolarization events, the MLT distribution could be

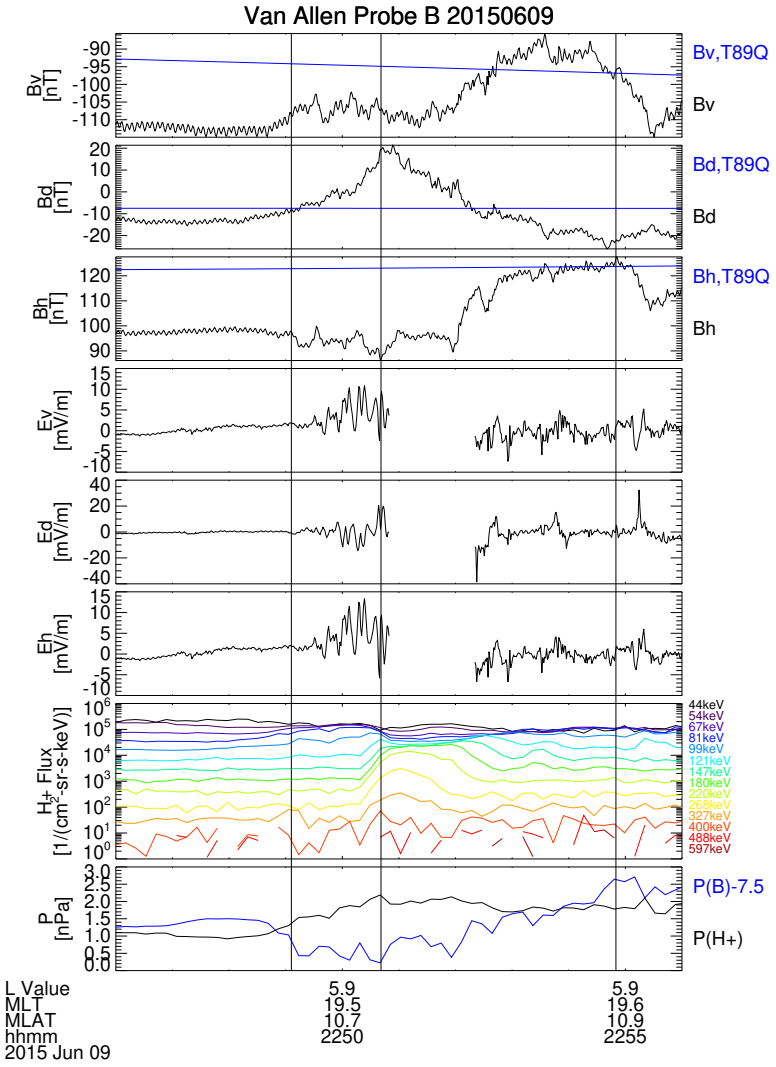

Figure 5. An overview plot for a dipolarization event starting at 22:50:41 UT on 9 June 2015, as observed by Van Allen Probe B. Magnetic fields, electric field, and energetic proton fluxes and pressure are plotted as in Figure 3. Three vertical lines indicate beginning of the dip, ending of the dip or beginning of the DF, and ending of the DF.

explained by these protons drifting westward in the inner magnetosphere. There is a slight tendency for events to be observed at lower L shells in the evening MLT. There are no significant features in the MLAT distribution. One possible reason is that Van Allen Probes' orbits were relatively close to the magnetic equator with $|\mathrm{MLAT}| < 20$ deg.

The distribution of geomagnetic indices (AU, AL, Kp, and Dst indices) at the MLT of each event is plotted in the right three panels. The events were observed during moderate auroral electrojet (AE) activities. AU values were as large as AL values in size so

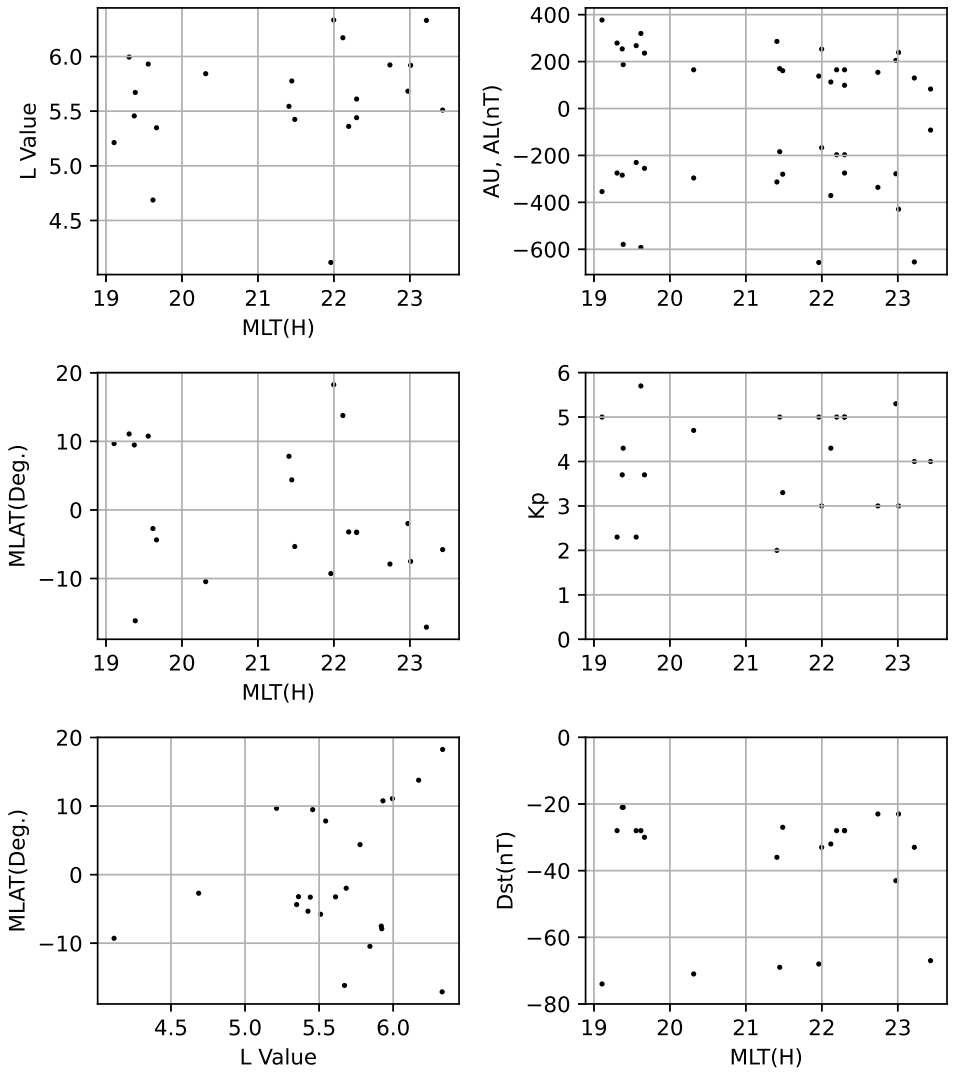

Figure 6. Left three panels show locations of dipolarization events organized by L value, MLT, or MLAT. Right three panels show geomagnetic activities (AU, AL, Kp, and Dst values) at MLT of each event.

that eastward electrojet was well developed. Since the eastward electrojet was expected in the duskside magnetosphere, westward convection was also expected there, which is a typical convection around that MLT during disturbed periods. Kp values were also moderate. Dst values of some events were < -50 nT, corresponding to geomagnetic storms, while those of other events were > -50 nT. Nonetheless, some minimum Dst values of these other events were < -50 nT around the time of the observation so that these events also occurred during storms. In summary, about 70 % of the events (16/22 events) were

storm-time events. This, together with moderate AE and Kp values, could account for the presence of dipolarization events at L shells inside geosynchronous orbit.

There is not much MLT dependence on geomagnetic activities. An exception could be the AU index. Events observed in the eveningside tend to have larger AU values. This could be due to well-developed eastward electrojet at that MLT. Perhaps, there was more proton flux transport from the magnetotail.

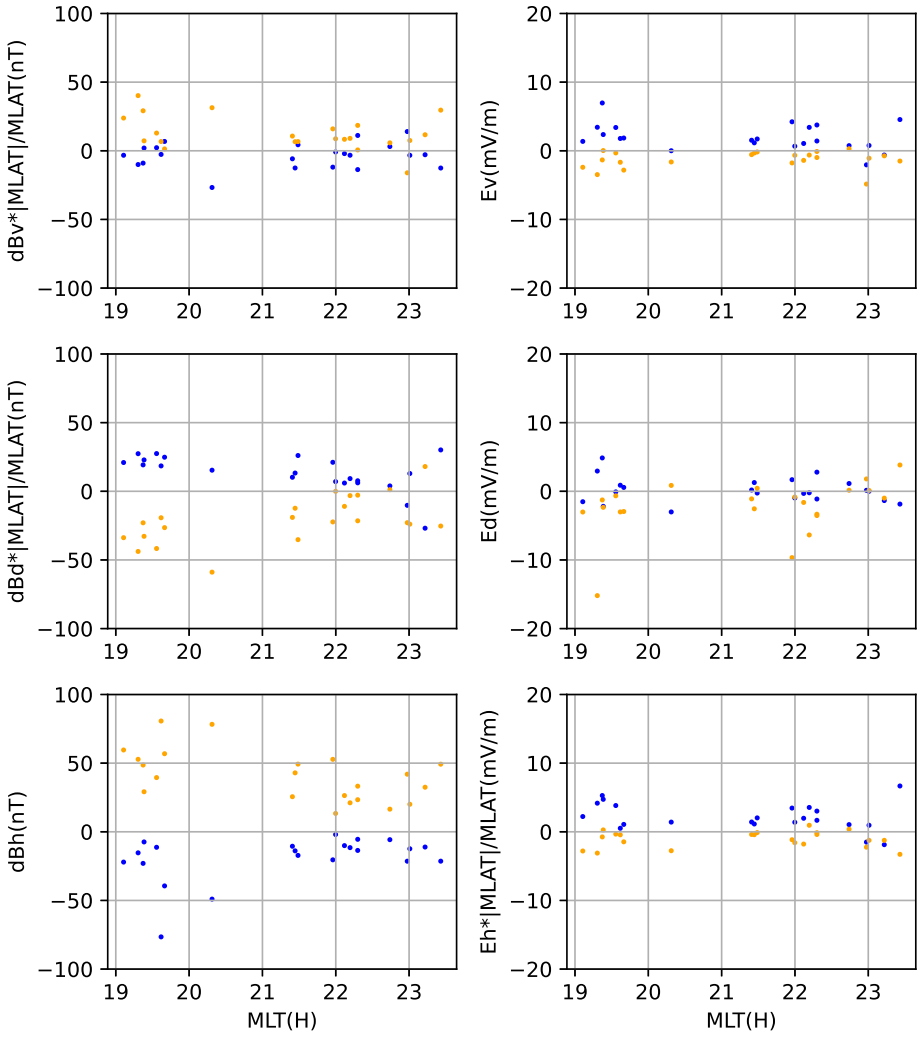

Figure 7. Distributions of each component of magnetic field variations and electric fields as a function of MLT. Blue and orange colors correspond to values calculated in the dip and DF, respectively. Signs of dB_V, dB_D, and E_H components in the southern hemisphere are reversed, assuming symmetry of the structures between the hemispheres.

Next we show distributions of magnetic field variations and electric fields derived for each event as a function of MLT (Figure 7). Magnetic field variations are calculated as differences between final and initial values in the dip (blue) and the DF (orange), respectively. Note that these colors are also used in later figures with the same meaning. Quiet-time model values B_{T89Q} have already been subtracted so that the definition is $dB \equiv (B - B_{T89Q})_{final} - (B - B_{T89Q})_{initial}$. Average electric fields are calculated in the dip and in the DF, respectively. These electric fields are contributed by variable components because averages are calculated for shorter time scales than large-scale, background convection changes affected by the magnetosphere-ionosphere (M-I) coupling. Note that there are partly gaps in electric field data in 7 of 22 events. Signs of dB_V, dB_D, and E_H components are reversed for the events in the southern hemisphere because of systematic inter-hemispheric differences, if the structure is symmetric between the hemispheres.

Signs of each field component were generally opposite between the dip and DF. Variations of magnetic fields were larger at an earlier MLT, which could be due to larger *AU* activities at that MLT, as mentioned before. Electric fields also had somewhat similar MLT dependence as magnetic field variations. There was a tendency for E_V and E_H components to be positive in the dip, while these were negative in the DF. This implies westward field line motion in the dip, while field lines moved back eastward in the DF. The medians of these electric fields are 2.2 mV/m in the dip and -1.6 mV/m in the DF. If converted to azimuthal $E\times B$ drift velocity, they are -17 km/s in the dip and 8 km/s in the DF. The former velocity is not far from the gradient B drift velocity of energetic protons so that these protons may be responsible for stretched field lines.

Signs of the dB_D component were generally the same as those of the E_V and E_H components, consistent with this idea of stretched field lines. Note that signs of the dB_D component are reversed in the southern hemisphere so that the magnetic field lines were likely displaced most at the equator, while they were tied to the ionosphere. For example, when field lines were moving westward at the equator, the electric field was outward. Eastward magnetic field increased in the northern hemisphere, while westward magnetic field did in the southern hemisphere. The shape of a field line was similar to that of fundamental-mode or odd harmonics of standing waves at least near the equator, where an anti-node was located. The possibility of standing waves is discussed later. The latitudinal dependence of the field line motion would be caused by energetic proton population trapped

around the equator. In addition, angular velocity of the gradient B/curvature drift of particles at an energy is the largest at the equator (Lew, 1961).

The E_D value was less than the E_V or E_H value in the dip. The median is -0.043 mV/m, while the median is -1.4 mV/m in the DF.

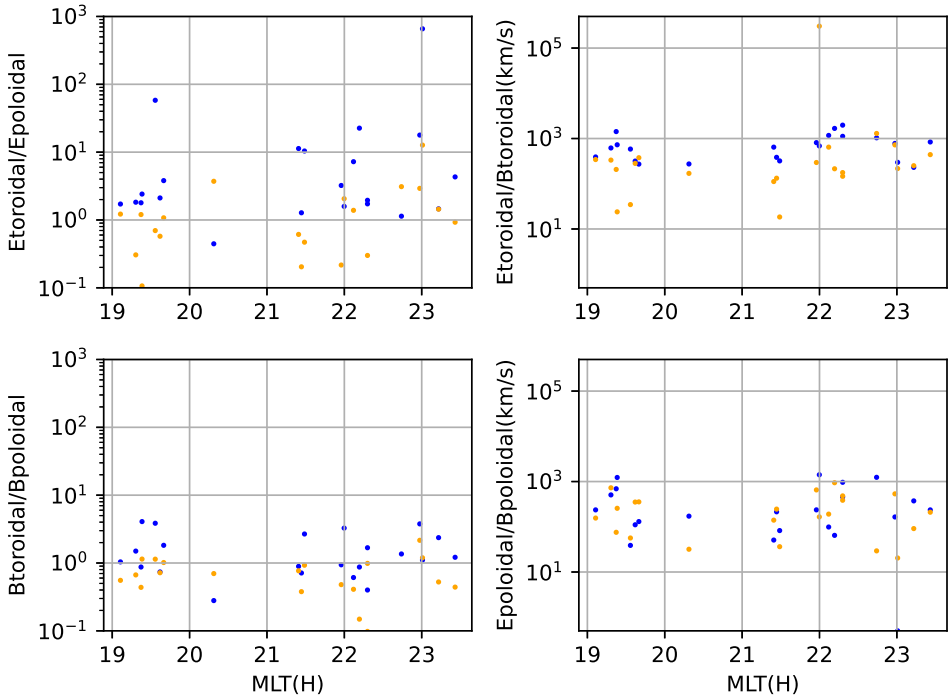

Figure 8. Left panels show ratios of toroidal components to poloidal components for magnetic fields (top) and electric fields (bottom). Right panels show E/B ratios of toroidal components (top) and poloidal components (bottom). Blue and orange colors correspond to the ratios at the dip and DF, respectively.

The ratios between toroidal and poloidal components are calculated for electric fields and magnetic fields (left panels of Figure 8). Toroidal electric fields are approximated to be in the plane perpendicular to the azimuthal direction and perpendicular to the background magnetic field component in that plane. Toroidal magnetic fields correspond to the azimuthal component. Poloidal electric fields are also the azimuthal component, while poloidal magnetic fields are defined in the same manner as the toroidal electric fields. The ratios were often > 1 for electric fields in the dip, implying the variations were mainly toroidal. The ratios for magnetic fields were ~ 1 because there were horizontal and ra-

dial magnetic field variations associated with the dip region itself in addition to the azimuthal ones. The ratios were smaller in the DF than in the dip. Electric fields in the DF were more westward in addition to the inward component. Magnetic field variations were more contributed by the horizontal and radial magnetic field increase.

Next, we discuss the E/B ratio calculated for toroidal and poloidal components (right panels in Figure 8). Since the ratio of averaged electric fields E and differentiated magnetic fields dB are not directly equivalent to the E/B ratio, we have multiplied a factor π to E/dB. The above factor applies to an ideal case when the variation is sinusoidal and may be divided into two parts. In the first part, the factor 2 is introduced because magnetic field variations are calculated as differences between maximum and minimum values, while electric field variations are assumed to have only one sign. Note that the phases between electric and magnetic fields are ideally shifted by 90 deg. In the second part, the additional factor $\pi/2$ is multiplied because electric fields assumed to be sinusoidal are averaged, while magnetic field variations are not. However, the actual case may be somewhat different so that the above factor is just only for reference.

There is not much MLT dependence of the E/B ratios. This is also the case for the MLAT dependence (figure not shown). The latter implies that the property of the structure to be inferred from this ratio, such as the spatial variation of standing waves, if any, in the field-aligned direction, does not change much inside the Van Allen Probes' orbits with $|\mathrm{MLAT}| < 20$ deg.

The toroidal E/B ratios in the dip were of the order of 1000 km/s or those of Alfvén waves at where events were observed (e.g., McPherron, 2005) (Figure 8, top right). Since there was a phase shift of ~ 90 deg. between electric and magnetic fields, the waves would not be propagating but standing. Nonetheless, the events were not likely to be solely the fundamental mode or odd harmonics of the standing waves. If that were the case, the E/B ratio would be larger than that of propagating waves near the equator. The E/B ratio was also similar to that of the ionospheric structure (e.g., Gurnett et al., 1984). However, electric fields and magnetic fields are in phase in this case (e.g., Smiddy et al., 1980) and we cannot explain the ~ 90 deg. phase shift.

Another possibility is that an injected energetic proton structure drifted and induced field line motion. This inference is applicable to stretched magnetic field lines discussed above. In this case, the E/B ratio is VB/dB. Even though the motional veloc-

ity V of field lines was smaller than the phase velocity of Alfvén waves, the magnetic field variation dB was also smaller than the background magnetic field B. A large range of values are possible for the E/B ratio, taking into account the dependence of this structure and its field line motion on latitudes. The phase shift may be ~ 90 deg. based on the spatial and temporal variation of this structure. Standing Alfvén waves may overlap. The E/B ratio contributed by the drifting structure and the standing waves would not necessarily be larger than the Alfvén velocity.

In the DF, the toroidal E/B ratio was smaller than that in the dip. The electric field decrease as well as the magnetic field increase contributed to the smaller ratio. Nonetheless, the drifting proton structure as well as standing waves possibly contributed to the observed E/B ratio, similar to the variations in the dip. On top of these structures and waves, there could be higher harmonics of standing waves in the DF because the field variations were irregular, particularly for electric fields as shown in the case study. The E/B ratio at higher frequencies up to 0.5 Hz is calculated and there was a tendency for this ratio to be larger than the one at lower frequencies derived above and to be closer to the typical Alfvén velocity (figure not shown). The larger E/B ratio is possibly because there was a larger contribution from higher harmonics to the field variations than the drifting energetic proton structures. Note that the E/B ratio is expected to be closer to the Alfvén velocity, if more harmonics overlap.

Standing waves during dipolarization events or substorms have previously been reported (Takahashi et al., 1988). Since the duration of the dip and DF was of the order of minutes or the Alfvén transit time between the magnetic equator and the ionosphere, there could be standing waves. Standing waves with kinetic effects during dipolarization events have been previously reported by Van Allen Probes (Chaston et al., 2014) and MMS (Matsui et al., 2016). Field variations are irregular in this case because there are multiple frequency or wavelength components. As already mentioned, electric field variations examined were irregular in the DF. In addition, parallel Poynting flux at higher frequencies up to 0.5 Hz is calculated and its standard deviations are larger than or close to average values. The direction of the Poynting flux along the magnetic field was variable, again implying that the field variation was irregular. Note also that the events studied here were observed by Van Allen Probes where the background magnetic field is dipole-like, in which Samson et al. (1992) inferred that there are standing waves with kinetic effects.

Concerning the poloidal E/B ratio (Figure 8, bottom right), the values were smaller than those of the toroidal ratio in the dip possibly because the electric field variation was mainly toroidal. In the DF, the poloidal ratio was similar to the toroidal ratio, implying the variation was more isotropic.

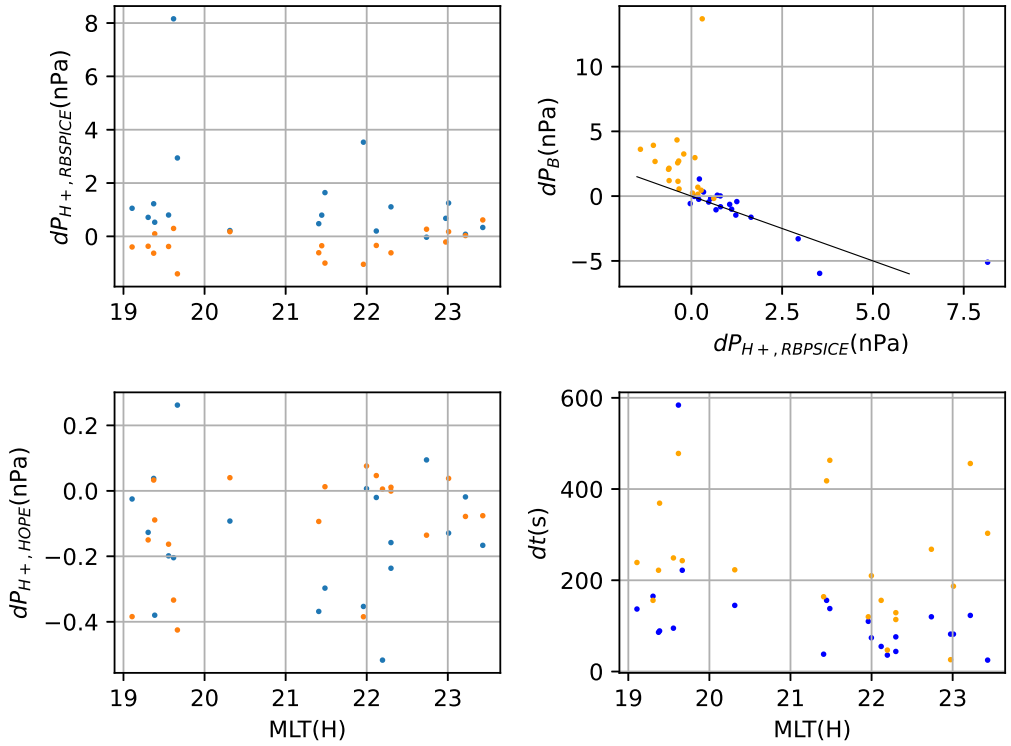

Figure 9. Left two panels show proton pressure variations either in the dip or DF, as measured by RBSPICE (top) and HOPE (bottom) and organized by MLT. The top right panel is a scatter plot between proton pressure variations measured by RBSPICE and magnetic pressure variations. The black line indicates where proton pressure variations are balanced by magnetic pressure variations with an opposite sign. The bottom right panel shows durations of the dip and DF as a function of MLT. The blue and orange colors in each panel correspond to the values in the dip and DF, respectively.

Proton pressure variations are derived in the RBSPICE energy range (40-800 keV) and the HOPE energy range (30 eV-50 keV) (Left two panels in Figure 9). Variations are calculated as differences between final and initial values in either the dip or DF. When there are no RBSPICE moments (3/22 events) or HOPE moments (2/22 events), we do not show results from each instrument. Proton pressure generally increased in the dip

in the RBSPICE energy range and decreased in the DF. Proton pressure decreased both in the dip and DF in the HOPE energy range. Proton pressure variations in the RBSPICE energy range were larger than those in the HOPE energy range. Proton pressure increases in the RBSPICE energy range were often balanced by magnetic pressure decreases in the dip (top right panel) so that total pressure did not change much. If the magnetic field variations gradually changed along magnetic field lines, the structure would be close to static. Proton pressure decreases were smaller than magnetic pressure increases in the DF so that the field variations were probably more variable in time than those in the dip. These proton pressure variations may contribute to a source term to generate Alfvén waves (Kivelson & Southwood, 1991). The idea of drifting particle structures, and in addition standing waves, inferred from the electric and magnetic field statistics, is consistent with this analysis.

Note that not all of the dipolarization events with inductive, radial electric fields are explained by the above idea of drifting energetic proton structure. For example, there were two events in the dip with $E_V < 0$ close to the midnight. Since proton pressure increased, these events may not be explained as the above. We have also checked whether electron pressure increased, supporting $E_V < 0$ because of the opposite drift direction to protons, but do not always find that signature. Some other explanation such as the radial variation of the structure, including the structure moving inward, needs to be introduced.

The bottom right panel of Figure 9 shows durations of the dip and DF as a function of MLT. These durations were generally longer in the earlier MLTs. Since there was a tendency for the background magnetic fields to be larger in the eveningside because of inner L shells of event locations, the observed durations could be explained by this effect, if the convection electric field did not change much with MLT. Another possibility is the difference in drift velocity between the middle-energy ions and the magnetic flux associated with the dipolarzation. The former is thought to be moving with the gradient B/curvature drift velocity in addition to the $E \times B$ drift velocity, while the latter is moving with the $E \times B$ drift velocity. Once the event arrives at the nightside inner magnetosphere from the magnetotail, the time difference between both structures increases as the MLT shifts toward the eveningside.

The longer durations of the dip in the eveningside could be consistent with Nagai (1982), in which the beginning of the B_H increase was more delayed from the substorm onset when a geosynchronous spacecraft was located further away from midnight. Note that the substorm onset in that study was identified by low- and middle-latitude ground magnetometers and was approximately simultaneous to the beginning of the azimuthal magnetic field variation. The coincidence of the beginning of the azimuthal magnetic field variation and that of the dip was observed in our case study.

If the longer duration of the dip in the eveningside would be caused by the different drift speed mentioned above, this may complement the explanation of the dip as being due to reflected ions at the DF in the magnetotail. This is because the reflection process would contribute to an offset to the dip durations, while their MLT dependence is due to the gradient B/curvature drift of middle-energy ions. Durations of the dip had offset values in the premidnight MLT in the figure.

Lastly, the MVA of magnetic fields (Sonnerup & Scheible, 1998) is performed to investigate characteristics of variable fields. An analysis period for an event includes the dip and DF. The L direction is defined to be positive in the northward direction, while the N direction is positive in the sunward direction. Eigenvalue ratios λ_1/λ_2 are larger in the evening MLT (top left panel of Figure 10), where λ_1 and λ_2 are maximum and intermediate eigenvalues, respectively. This is related to larger fluctuations in B_H and B_D components around this MLT. These ratios decrease in the premidnight MLT, while the ratios λ_2/λ_3 tend to increase. Here λ_3 is a minimum eigenvalue. Fluctuations were more two-dimensional in the plane including H and D directions. Angles of L and N directions from the background magnetic fields are calculated when $\lambda_1/\lambda_2 > 3$ and $\lambda_2/\lambda_3 > 3$, respectively (bottom left panel). L directions tend to be parallel to the background fields near the equator at |MLAT| $<\sim$ 5 deg. and perpendicular outside the equator. N directions are perpendicular to the background fields near the equator and parallel outside the equator. Therefore, dipolarizations were more compressional near the equator, while magnetic variations were more transverse off the equator possibly because of larger background magnetic fields along a magnetic field line.

Elevation and azimuth angles of L directions are plotted in VDH coordinates when $\lambda_1/\lambda_2 > 3$ and L directions are quasi-perpendicular $>$ 45 deg. to background magnetic fields (top right panel). Azimuth angles are often $\sim$ 90 deg., implying that maximum

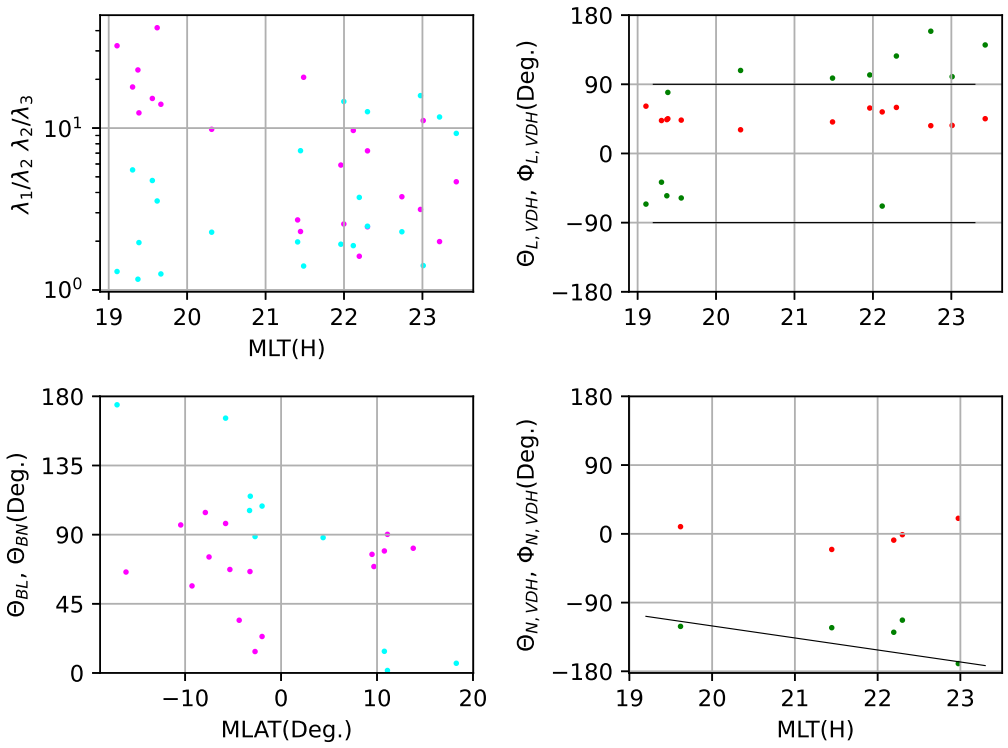

Figure 10. Results from the minimum variance analysis (MVA) for our dipolarization events. The top left panel shows eigenvalue ratios λ_1/λ_2 and λ_2/λ_3 as a function of MLT in magenta and cyan colors, respectively. The bottom left panel shows angles of L and N directions from background magnetic fields as a function of MLAT in magenta and cyan colors, when $\lambda_1/\lambda_2 > 3$ and $\lambda_2/\lambda_3 > 3$, respectively. The right two panels show L and N directions in VDH coordinates as a function of MLT, when the above condition for eigenvalue ratios is satisfied and directions are $>$ 45 deg. from background magnetic fields. Elevation and azimuth angles are plotted in red and green colors, respectively. Black lines indicate where L directions are azimuthal (top right panel) and N directions are sunward (bottom right panel).

variations include azimuthal variations related to field-line stretching off the equator. Similarly, elevation and azimuth angles of N directions are plotted when $\lambda_2/\lambda_3 > 3$ and N directions are quasi-perpendicular (bottom right panel). Azimuth angles tend to align to the X or D direction. It is hard to distinguish between these because number of data points is not large. This implies the structure propagated in the sunward or westward direction.

5 Summary and Conclusions

Two case studies of dipolarization events with inductive, radial electric fields were presented. In addition, a total of 22 dipolarization events have been collected and statistically analyzed. These events were observed between evening and premidnight MLTs and were accompanied by energetic proton increases. When there were no RBSPICE data, MAGEIS instruments, also measuring ions, observed such increases > 60 or > 160 keV. The events occurred during moderate geomagnetic activities. About 70 % of them corresponded to geomagnetic storms. In general, signs of each component of magnetic and electric field variations were opposite between the dip and DF. Field line motion in the dip was similar to the gradient B/curvature drift velocities of energetic protons. Plasma pressure increased in the dip and decreased in the DF. Durations of the DF were longer in the earlier MLT. According to the MVA, variations were more compressional near the equator.

Below is one possible explanation for the overall characteristics of magnetic and electric field variations and energetic protons in the dip. Since these magnetic field variations appeared with energetic proton injections and the field line motion was similar to the gradient B/curvature drift velocities of these protons, the field line would be stretched by these protons. One possibility is that these energetic protons were reflected at the DF in the magnetotail and subsequently transported to the inner magnetosphere. Referring to the azimuthal magnetic field variation which was opposite between hemispheres, the magnetic field line was most stretched westward around the equator. This is because there were trapped energetic populations with their largest drift around the equator. Fundamental mode or odd harmonics of standing waves could be generated.

In the DF, field variations were more irregular. It is inferred that there were standing waves with higher harmonics. Convection turned to eastward in the DF possibly because field lines may not be stretched further. The field lines previously in the dip may collide with those in the westward location so that magnetic and electric field variations may become turbulent with kinetic effects. The horizontal magnetic field started to increase with energetic protons for the event on 9 June 2015. The energy was larger than that of middle-energy protons in the dip. The higher-energy protons near the minimum B_H would be accelerated by local processes, such as the interaction of populations trapped around the DF with electric field induced by the DF motion (Ukhorskiy et al., 2017).

Possible future study may be performed with MMS data set (Burch et al., 2016), which is now growing. Multi-spacecraft data analyses such as the timing analysis and the curlometer technique could work. Sub-ion scale structures may also be analyzed. Although low-energy populations are often not measured, these do not contribute much to the pressure in the inner magnetosphere so that analyses with high-energy populations would be sufficient.

6 Open Research

Van Allen Probes data are publicly available at https://emfisis.physics.uiowa.edu/, http://space.umn.edu/missions/rbspefw-home-university-of-minnesota/, http://rbspice.ftecs.com/, and https://cdaweb.gsfc.nasa.gov/. AE and Dst indices are available at https://wdc.kugi.kyoto-u.ac.jp/ (Nose et al., 2015a, 2015b). Kp index may be downloaded at https://www.gfz-potsdam.de/en/kp-index/ (Matzka, Bronkalla, et al., 2021). OMNI data are available at https://omniweb.gsfc.nasa.gov/ (Papitashvili & King, 2020).

The data analysis software to generate figures in this study is available on Zenodo (Matsui & Farrugia, 2022).

Acknowledgments

This work was supported by NASA's Van Allen Probes Contract NAS5-01072 and NASA Grant 80NSSC22K0526.

References

Baker, D. N., Belian, R. D., Higbie, P. R., & Hones, E. W., Jr. (1979). High-energy magnetospheric protons and their dependence on geomagnetic and interplanetary conditions. *Journal of Geophysical Research*, *84*, 7138–7154. doi: https://doi.org/10.1029/JA084iA12p07138

Birn, J., Thomsen, M. F., Borovsky, J. E., Reeves, G. D., McComas, D. J., & Belian, R. D. (1997). Characteristic plasma properties during dispersionless substorm injections at geosynchronous orbit. *Journal of Geophysical Research*, *102*, 2309–2324. doi: https://doi.org/10.1029/96JA02870

Blake, J. B., Carranza, P. A., Claudepierre, S. G., Clemmons, J. H., Crain, W. R., Jr., Dotan, Y., et al. (2013). The Magnetic Electron Ion Spectrometer

(MagEIS) instruments aboard the Radiation Belt Storm Probes (RBSP) spacecraft. *Space Science Reviews*, *179*, 383–421. doi: https://doi.org/10.1007/s11214-013-9991-8

Burch, J. L., Moore, T. E., Torbert, R. B., & Giles, B. L. (2016). Magnetospheric Multiscale overview and science objectives. *Space Science Reviews*, *199*, 5–21. doi: https://doi.org/10.1007/s11214-015-0164-9

Chaston, C. C., Bonnell, J. W., Wygant, J. R., Mozer, F., Bale, S. D., Kersten, K., et al. (2014). Observations of kinetic scale field line resonances. *Geophysical Research Letters*, *41*, 209–215. doi: https://doi.org/10.1002/2013GL058507

Cummings, W. D., Barfield, J. N., & Coleman, P. J., Jr. (1968). Magnetospheric substorms observed at the synchronous orbit. *Journal of Geophysical Research*, *73*, 6687–6698. doi: https://doi.org/10.1029/JA073i021p06687

Ergun, R. E., Goodrich, K. A., Stawarz, J. E., Andersson, L., & Angelopoulos, V. (2015). Large-amplitude electric fields associated with bursty bulk flow breaking in the Earth's plasma sheet. *Journal of Geophysical Research: Space Physics*, *120*, 1832–1844. doi: https://doi.org/10.1002/2014JA020165

Funsten, H. O., Skoug, R. M., Guthrie, A. A., MacDonald, E. A., Baldonado, J. R., Harper, R. W., et al. (2013). Helium, Oxygen, Proton, and Electron (HOPE) mass spectrometer for the Radiation Belt Storm Probes mission. *Space Science Reviews*, *179*, 423–484. doi: https://doi.org/10.1007/s11214-013-9968-7

Gkioulidou, M., Ohtani, S., Mitchell, D. G., Ukhorskiy, A. Y., Reeves, G. D., Turner, D. L., et al. (2015). Spatial structure and temporal evolution of energetic particle injections in the inner magnetosphere durng the 14 July 2013 substorm event. *Journal of Geophysical Research: Space Physics*, *120*, 1924–1938. doi: https://doi.org/10.1002/2014JA020872

Gurnett, D. A., Huff, R. L., Menietti, J. D., Burch, J. L., Winningham, J. D., & Shawhan, S. D. (1984). Correlated low-frequency electric and magnetic noise along the auroral field lines. *Journal of Geophysical Research*, *89*, 8971–8985. doi: https://doi.org/10.1029/JA089iA10p08971

Kepko, L., McPherron, R. L., Amm, O., Apatenkov, S., Baumjohann, W., Birn, J., et al. (2015). Substorm current wedge revisited. *Space Science Reviews*, *190*, 1–46. doi: https://doi.org/10.1007/s11214-014-0124-9

King, J. H., & Papitashvili, N. E. (2005). Solar wind spatial scales in and com-

parisons of hourly Wind and ACE plasma and magnetic field data. *Journal of Geophysical Research*, *110*, A02104. doi: https://doi.org/10.1029/2004JA010649

Kivelson, M. G., & Southwood, D. J. (1991). Ionospheric traveling vortex generation by solar wind buffeting of the magnetosphere. *Journal of Geophysical Research*, *96*, 1661–1667. doi: 10.1029/90JA01805

Kletzing, C. A., Kurth, W. S., Acuna, M., MacDowall, R. J., Torbert, R. B., Averkamp, T., et al. (2013). The Electric and Magnetic Field Instrument Suite and Integrated Science (EMFISIS) on RBSP. *Space Science Reviews*, *179*, 127–181. doi: https://doi.org/10.1007/s11214-013-9993-6

Lew, J. S. (1961). Drift rate in a dipole field. *Journal of Geophysical Research*, *66*, 2681–2685. doi: https://doi.org/10.1029/JZ066i009p02681

Liu, J., Angelopoulos, V., Zhang, X.-J., Turner, D. L., Gabrielse, C., Runov, A., et al. (2016). Dipolarizing flux bundles in the cis-geosynchronous magnetosphere: Relationship between electric fields and energetic particle injections. *Journal of Geophysical Research: Space Physics*, *121*, 1362–1376. doi: https://doi.org/10.1002/2015JA021691

Matsui, H., Erickson, P. J., Foster, J. C., Torbert, R. B., Argall, M. R., Anderson, B. J., et al. (2016). Dipolarization in the inner magnetosphere during a geomagnetic storm on 7 October 2015. *Geophysical Research Letters*, *43*, 9397–9405. doi: https://doi.org/10.1002/2016GL070677

Matsui, H., & Farrugia, C. J. (2022). *Data Analysis Software for Dipolariation Events With Inductive, Radial Electric Fields Observed by Van Allen Probes. V. 1.0. [Software].* Zenodo. doi: https://doi.org/10.5281/zenodo.7261397

Matzka, J., Bronkalla, O., Tornow, K., Elger, K., & Stolle, C. (2021). *Geomagnetic Kp index. V. 1.0. [Dataset].* GFZ Data Services. doi: https://doi.org/10.5880/Kp.0001

Matzka, J., Stolle, C., Yamazaki, Y., Bronkalla, O., & Morschhauser, A. (2021). The geomagnetic *Kp* index and derived indices of geomagnetic activity. *Space Weather*, *19*, e2020SW002641. doi: https://doi.org/10.1029/2020SW002641

Mauk, B. H., Fox, N. J., Kanekal, S. G., Kessel, R. L., Sibeck, D. G., & Ukhorskiy, A. (2013). Science objectives and rationale for the Radiation Belt Storm Probes mission. *Space Science Reviews*, *179*, 3–27. doi: https://doi.org/

10.1007/s11214-012-9908-y

McPherron, R. L. (2005). Magnetic pulsations: Their sources and relation to solar wind and geomagnetic activity. *Surveys in Geophysics*, *26*, 545–592. doi: https://doi.org/10.1007/s10712-005-1758-7

McPherron, R. L., Russell, C. T., & Aubry, M. P. (1973). Satellite studies of magnetospheric substorms on August 15, 1968 9. Phenomenological model for substorms. *Journal of Geophysical Research*, *78*, 3131–3149. doi: https://doi.org/10.1029/JA078i016p03131

Mitchell, D. G., Lanzerotti, L. J., Kim, C. K., Stokes, M., Ho, G., Cooper, S., et al. (2013). Radiation Belt Storm Probes Ion Composition Experiment (RBSPICE). *Space Science Reviews*, *179*, 263–308. doi: https://doi.org/10.1007/s11214-013-9965-x

Motoba, T., Ohtani, S., Gkioulidou, M., Ukhorskiy, A. Y., Lanzerotti, L. J., & Claudepierre, S. G. (2021). Superposed epoch analysis of dispersionless particle injections inside geosynchronous orbit. *Journal of Geophysical Research: Space Physics*, *126*, e2021JA029546. doi: https://doi.org/10.1029/2021JA029546

Nagai, T. (1982). Observed magnetic substorm signatures at synchronous altitude. *Journal of Geophysical Research*, *87*, 4405–4417. doi: https://doi.org/10.1029/JA087iA06p04405

Nakamura, R., Baumjohann, W., Klecker, B., Bogdanova, Y., Balogh, A., Rème, H., et al. (2002). Motion of the dipolarization front during a flow burst event observed by Cluster. *Geophysical Research Letters*, *29*, 1942. doi: https://doi.org/10.1029/2002GL015763

Nose, M., Iyemori, T., Sugiura, M., & Kamei, T. (2015a). *Geomagnetic AE index.* World Data Center for Geomagnetism, Kyoto. doi: https://doi.org/10.17593/15031-54800

Nose, M., Iyemori, T., Sugiura, M., & Kamei, T. (2015b). *Geomagnetic Dst index.* World Data Center for Geomagnetism, Kyoto. doi: https://doi.org/10.17593/14515-74000

Papitashvili, N. E., & King, J. H. (2020). *OMNI 1-min Data [Dataset].* NASA Space Physics Data Facility. doi: https://doi.org/10.48322/45bb-8792

Runov, A., Angelopoulos, V., Zhou, X.-Z., Zhang, X.-J., Li, S., Plaschke, F., & Bonnell, J. (2011). A THEMIS multicase study of dipolarization fronts in the

magnetotail plasma sheet. *Journal of Geophysical Research*, *116*, A05216. doi: https://doi.org/10.1029/2010JA016316

Samson, J. C., Wallis, D. D., Hughes, T. J., Creutzberg, F., Ruohoniemi, J. M., & Greenwald, R. A. (1992). Substorm intensifications and field line resonances in the nightside magnetosphere. *Journal of Geophysical Research*, *97*, 8495–8518. doi: https://doi.org/10.1029/91JA03156

Schmid, D., Volwerk, M., Plaschke, F., Nakamura, R., Baumjohann, W., Wang, G. Q., et al. (2019). A statistical study on the properties of dips ahead of dipolarization fronts observed by MMS. *Journal of Geophysical Research: Space Physics*, *124*, 139–150. doi: https://doi.org/10.1029/2018JA026062

Sergeev, V. A., Angelopoulos, V., & Nakamura, R. (2012). Recent advances in understanding substorm dynamics. *Geophysical Research Letters*, *39*, L05101. doi: https://doi.org/10.1029/2012GL050859

Smiddy, M., Burke, W. J., Kelley, M. C., Saflekos, N. A., Gussenhoven, M. S., Hardy, D. A., & Rich, F. J. (1980). Effects of high-latitude conductivity on observed convection elelctric fields and Birkeland currents. *Journal of Geophysical Research*, *85*, 6811–6818. doi: https://doi.org/10.1029/JA085iA12p06811

Sonnerup, B. U. O., & Scheible, M. (1998). Minimum and maximum variance analysis. In G. Paschmann & P. W. Daly (Eds.), *Analysis methods for multispacecraft data* (pp. 185–220). Noordwijk, The Netherlands: ESA Publications Division.

Takahashi, K., Kokubun, S., Sakurai, T., McEntire, R. W., Potemra, T. A., & Lopez, R. E. (1988). AMPTE/CCE observations of substorm-associated standing Alfvén waves in the midnight sector. *Geophysical Research Letters*, *15*, 1287–1290. doi: https://doi.org/10.1029/GL015i011p01287

Tian, S., Colpitts, C. A., Wygant, J. R., Cattell, C. A., Ferradas, C. P., Igl, A. B., et al. (2021). Evidence of Alfvenic Poynting flux as the primary driver of auroral motion during a geomagnetic substorm. *Journal of Geophysical Research: Space Physics*, *126*, e2020JA029019. doi: https://doi.org/10.1029/2020JA029019

Tsyganenko, N. A. (1989). A magnetospheric magnetic field model with the warped tail current sheet. *Planetary and Space Science*, *37*, 5–20. doi: https://doi.org/10.1016/0032-0633(89)90066-4

Ukhorskiy, A. Y., Sitnov, M. I., Merkin, V. G., Gkioulidou, M., & Mitchell, D. G. (2017). Ion acceleration at dipolarization fronts in the inner magnetosphere. *Journal of Geophysical Research: Space Physics*, *122*, 3040–3054. doi: https://doi.org/10.1002/2016JA023304

Wygant, J. R., Bonnell, J. W., Goetz, K., Ergun, R. E., Mozer, F. S., Bale, S. D., et al. (2013). The Electric Field and Waves instruments on the Radiation Belt Storm Probes mission. *Space Science Reviews*, *179*, 183–220. doi: https://doi.org/10.1007/s11214-013-0013-7

Zhou, X.-Z., Angelopoulos, V., Liu, J., Runov, A., & Li, S.-S. (2014). On the origin of pressure and magnetic perturbations ahead of dipolarization fronts. *Journal of Geophysical Research: Space Physics*, *119*, 211–220. doi: https://doi.org/10.1002/2013JA019394

Zhou, X.-Z., Angelopoulos, V., Sergeev, V. A., & Runov, A. (2011). On the nature of precursor flows upstream of advancing dipolarization fronts. *Journal of Geophysical Research*, *116*, A03222. doi: https://doi.org/10.1029/2010JA016165